Improving the transferability of density functional theory predictions through correlation analysis: Structural and energetic properties of NiX alloys (X = C, Si, Ge, and Sn)

Ageo Meier de Andrade ⬤, Jolla Kullgren, and Peter Broqvist ⬤[*]

Department of Chemistry - Ångström Laboratory, Uppsala University, Sweden

This work reports on the performance of density functional theory (DFT) for a series of single and binary systems, aiming for a quantitative description of NiX (X = C, Si, Ge, and Sn) alloys. Both semilocal GGA and a meta-GGA density functional, with and without dispersion corrections, are tested. We found in our study that no single functional simultaneously provides an accurate quantitative description of the investigated structural and energetic properties. However, the spread in computed DFT data could be rationalized in terms of the distribution of reduced density gradients and differences in the evolution of the exchange enhancement factors for different functionals. We demonstrate how to construct a regression model based on data from several density functionals that increases the predictivity of semilocal DFT. We foresee that the use of regression models (or extensions of it) can be valuable in the development of more accurate density functionals that in the future could provide a quantitative accuracy for complex multicomponent systems.

I. INTRODUCTION

Metal alloys are used in a wide range of applications owing to the possibility of tailoring the composition and atomic structure and optimizing material properties to fit desired usage areas. In the field of materials science, one classic example is the reinforcement of steel in the carbon-iron system, promoted by interstitial carbon atoms in the iron matrix. There also exist other successful examples of alloys with elements from group 14, commonly used in various technological applications. Transition metal silicides are used as corrosion-resistant materials and as coatings in semiconductor devices [1,2], transition metal germanites are interesting for their versatile electrical and magnetic properties [3–5], and a stannate alloy is the most successful example of a lead-free solder in microelectronic applications [6,7]. Transition metal nanoparticles alloyed with tin have also gained some attention in the field of heterogeneous catalysis. In particular, tin alloying has been observed to improve the selectivity for certain hydrogenation reactions [8–10]. Even though alloys are commonly used in many fields, it is still challenging to predict the origin of synergistic effects from different constituents using experiments alone. Here, theoretical calculations have an important role to fill, which is to gain insight into the often complex interplay between the different involved elements and their impact on various alloy properties.

Theoretical endeavors in the field of alloying are often performed using various multiscale approaches with the density functional theory (DFT) serving as input for more approximate methods [11,12]. Examples of such more approximate methods commonly used for predicting properties of alloys are the cluster expansion model [13] and the modified embedded atom method (MEAM) [14–17]. These less computationally demanding methods enable researchers to reach another level of size and time scales than using DFT, which is necessary to obtain the statistics needed to account for entropic effects in alloy systems. For example, such approaches can be used to compute thermodynamic quantities in conjunction with the CALPHAD approach to derive phase diagrams [18,19]. However, to be successful in such applications, we need a theory that accurately describes *all* different phases of a material, at *all* different compositions.

One problem when using DFT for complex chemical bonding situations (e.g., combinations of metallic, covalent, and ionic bonds) is that standard approximations, which often serve as the basis in many multiscale approaches, are usually of insufficient accuracy. Working with materials that display a broad spectrum of possible chemical bonds makes it challenging for modelers to choose the most appropriate density functional to use [20]. In such cases, the classification scheme of Perdew and co-workers, who introduced the *so-called* Jacob's ladder to visualize the approximations used in different density functionals when it comes to the exchange energy, serves as a helpful guide [21]. In analogy to Jacob's ladder, they proposed a link between the earth (being the Hartree world) and heaven where chemical accuracy is obtained. Klimeš and Michaelides provided a similar view for the inclusion of dispersion (nonlocal correlation) [22]. In these views, each rung in the ladder corresponds to a level of approximation, and a modeler can easily determine the approximations being used. At the first rung, the local density approximation (LDA) [23] is found, and the functional heaven is reached when the functional form is exact, without any approximations. The rung closest to heaven comprises the random phase

---
[*]peter.broqvist@kemi.uu.se

approximation (RPA) [24], which includes accurate models for both exchange and correlation. Between the first and last rungs, the functionals are classified based on how they deal with the exchange energy through the generalized gradient approximation (GGA, second rung), meta-GGA approximation (third rung), and hybrid functionals (fourth rung). At all these rungs, side tracks adding dispersion corrections can be made, each with its own set of rungs with different approximations to compute the contribution from nonlocal correlation. Dispersion corrections start with a force field as the Grimme D(1-3) methods, and they correspond to the first (where pairwise coefficients are isotropic with respect to the chemical environment) and second (where pairwise coefficients depend on the effective volume of the atom) rungs in the ladder [25–27]. The third rung comprises a set of functionals where dispersion corrections are included explicitly into the density functional through the use of a kernel. These functionals are called van der Waals density functionals (vdW-DF), and they offer means of computing dispersion interactions self-consistently at an affordable computational cost [28,29]. In Jacob's ladder for dispersion corrections, the fourth rung and beyond account for dispersion interactions through many-body terms [30–32].

To make an educated choice of which density functional is suitable for a certain material and property, it is essential to understand how functionals are constructed and in what respect they differ. One strategy here is to identify trends in calculated quantities with respect to the gradient correction to the exchange energy, the so-called exchange enhancement factor, which introduces a gradient dependence via the reduced density gradient $s[\rho(\mathbf{r})]$. In theoretical chemistry, $s[\rho(\mathbf{r})]$ is often used to quantify chemical bonding in molecular systems [33–35]. Furthermore, $s[\rho(\mathbf{r})]$ have also been used to pinpoint desirable features of GGA or vdW-DF density functionals [36]. In a previous attempt to increase the awareness about the performance of different classes of density functionals in their capability of predicting properties of materials, we used the distribution of reduced density gradients to rationalize among differences in structural and energetic bulk and surface properties computed with different density functionals [37]. In Ref. [37], nickel (Ni) in various forms (bulk, surface, and atom) represented the different reduced density gradient distributions. In the current contribution, we introduce another level of complexity by considering Ni bulk alloys. Similarly, we investigate the different chemical bonding in bulk materials and determine the most important ingredients for an accurate description of alloys with different bond characters. We focus our discussion on the role of exchange and dispersion interactions in the description of physical and chemical properties of the single- and multicomponent systems of Ni alloys with group 14 elements of the periodic table [carbon (C), silicon (Si), germanium (Ge), and tin (Sn)].

II. THEORETICAL METHODS

A. Exchange-correlation functionals and dispersion corrections

A key factor controlling the accuracy of a DFT functional is how the exchange-correlation energy is formulated. This work focuses on density functionals constructed based on the GGA
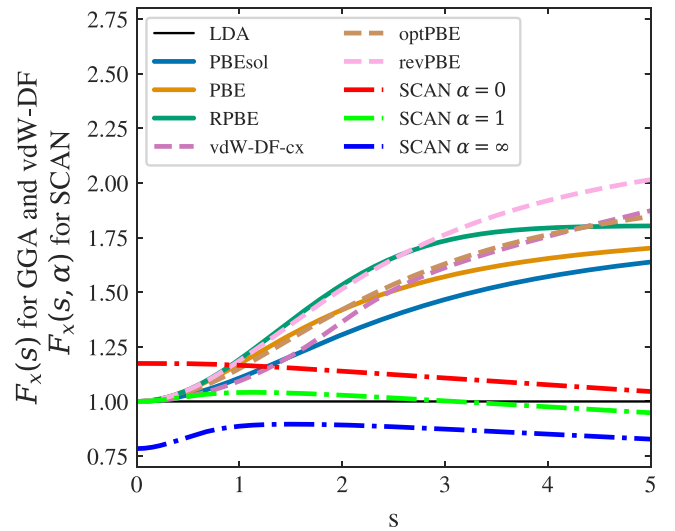

FIG. 1. Exchange enhancement factor $F_x(s)$ as a function of the reduced density gradient s for the GGA (solid lines) and vdW-DF (dashed lines) functionals studied in this work and for SCAN (dash-dot lines) with different values of α. LDA (solid black line) serves as a baseline when comparing these functionals.

approximation, where the exchange and correlation energies are treated separately. In such a formalism, the exchange energy is typically written as:

$$E_x^{\mathrm{GGA}} = \int d\mathbf{r}\,\rho(\mathbf{r})\epsilon_x^{\mathrm{unif}}F_x(s), \qquad (1)$$

where $\rho(\mathbf{r})$ is the total electron density, $\epsilon_x^{\mathrm{unif}}$ is the exchange energy from the uniform electron gas, and $F_x(s)$ is the exchange enhancement factor, which is a function of s, the dimensionless reduced density gradient given by:

$$s = \frac{1}{2(3\pi^2)^{1/3}}\frac{\nabla\rho(\mathbf{r})}{\rho^{4/3}(\mathbf{r})}. \qquad (2)$$

A broad range of GGA functionals differ only in the way that $F_x(s)$ is expressed between the limits of low s values, which results in an LDA formalism ($s = 0$) and high values where $F_x(s)$ should level out to the so-called Lieb-Oxford limit [38]. However, not all functionals fulfill this basic demand at high s values. In fact, it is not clear if this is actually needed for a "good" functional, as it add constraints on the shape of $F_x(s)$ for intermediate s values. It is, however, clear that different chemical bonding (metallic, ionic, or covalent), i.e., localized or delocalized Kohn-Sham orbitals (large or small electron density gradients), require different $F_x(s)$ functions. This is illustrated in Fig. 1, where the solid lines show the $F_x(s)$ computed using the Perdew-Burke-Ernzerhof (PBE) formulation [39,40] together with two variants where the "shape" has been optimized for solids (PBEsol) [41] and for molecules (revised PBE, RPBE) [42]. In this respect, the PBE functional can be seen as a compromise, being equally good when applied on both solids and molecules. To perform better for molecules, a faster increase (higher functional steepness) in $F_x(s)$ compared to the one in PBE is needed. On the other hand, a lower steepness is required to better describe solids (cf. Fig. 1). As such, it is not easy to formulate a GGA density

functional that simultaneously performs equally accurate for a broad range of *s* values.

Another class of functionals, which adds more flexibility in the formalism, is the meta-GGA functionals. These functionals additionally account for the electron kinetic energy density, which gives extra degrees of freedom when it comes to computing an effective $F_x(s)$ (in the language of GGA's). In principle, these additions allow $F_x(s)$ to change shape depending on the local chemistry described by the local kinetic energy density. In materials science, the strongly constrained and appropriately normed (SCAN) functional [43] has been brought forward since it is one of the most successful meta-GGAs in describing materials properties. Therefore, we have chosen this functional to represent the meta-GGA level of approximation. The exchange enhancement factor for SCAN is a function of two variables, s and α, enabling SCAN to recognize different bonding characters, e.g., covalent when $\alpha = 0$, metallic when $\alpha = 1$, and weak interactions when $\alpha = \infty$. Since the exchange enhancement factor for SCAN is a function of two variables, $F_x^{\mathrm{SCAN}}(s, \alpha)$ does not take the form of a single function as for GGA functionals, as seen in the dash-dot lines in Fig. 1. As such, this functional often provides higher accuracy for a broader set of chemical bonding situations.

Neither GGA nor meta-GGA functionals account for long-range dispersion interactions, and the total energy must be corrected if one wants to account for such interactions in the calculations. In this work, two ways to include dispersion corrections were considered, either through an *a posteriori* correction or using a self-consistent approach with the nonlocal correlation explicitly accounted for within the density functional. For the *a posteriori* correction, Grimme's DX ($x = 1$ to 3) is one of the most common approaches to account for dispersion interactions in computational chemistry, and the D3 dispersion correction [27] was used in our calculations in conjunction with the same set of GGA functionals described above (PBE, PBEsol, and RPBE). In the self-consistent approaches, the so-called vdW-DF functionals [44–46], the exchange and correlation energy is expressed according to:

$$E_{xc}^{\mathrm{vdW\text{-}DF}} = E_x^{\mathrm{GGA}} + E_c^{\mathrm{LDA}} + E_c^{nl}, \qquad (3)$$

where dispersion interactions are accounted for self-consistently through the nonlocal correlation term E_c^{nl} computed using a precalculated kernel. As for GGA functionals, there exists a large pool of different vdW-DF functionals, which differ in terms of how their exchange enhancement factor is formulated and in turn how E_x^{GGA} is calculated. In this work, a set of vdW-DF type of functionals that provide a good balance between accuracy and computational cost were selected based on findings in Ref. [37]. The exchange enhancement factor of these functionals (revPBE-vdW, vdW-DF-cx, and optPBE-vdW) are shown by the dashed lines in Fig. 1.

Dispersion corrections can also be used together with a meta-GGA functional, even though some short- and intermediate-ranged dispersion interactions have been claimed to be already accounted for in these functionals. For example, SCAN is commonly used with the revised Vydrov and van Voorhis kernel (SCAN-rVV10) as described

in Ref. [47]. Since one of the goals of this work is to investigate how dispersion corrections affect the accuracy of DFT, results from SCAN-rVV10 were also included. For further details concerning different approximations for E_{xc} and dispersion corrections in DFT, the reader is referred to Refs. [21,22,48,49].

B. Computational details

Spin-polarized calculations were performed based on density functional theory in the implementation with plane waves and pseudopotentials using the Vienna *ab initio* simulation package (VASP) [50–53]. Projected augmented wave (PAW) pseudopotentials were used in all calculations [54,55]. The $4s^2 3d^8$ for Ni, and $ns^2 np^2$, where n is the main quantum number for C, Si, Ge, and Sn, were treated as valence electrons. The pseudopotentials were obtained from the VASP library and are generated using the PBE density functional. For consistency, the same pseudopotential for a given element was used regardless of the chosen functional. Nonspherical contributions from the gradient corrections inside the PAW spheres were included in all calculations.

Structural optimizations of the unit cell and atomic positions for all bulk systems were performed using the conjugate gradient algorithm [56], where the relaxation continued until all components of the stress tensor were less than 0.01 kBar and the forces on each atom were less than 0.01 eV/Å. The Brillouin zone was sampled using a k spacing of 0.2 Å^{-1} for all bulk and alloy compounds. In all calculations, the plane wave energy cutoff was set to 600 eV.

C. Structural models

A series of structural models of single-component and alloy phases were investigated in this work. For the single-component systems, we considered the thermodynamically most stable low-temperature phases that have been found experimentally. This implies Ni in its face-centered cubic (fcc) phase, C in its graphitic phase, and the diamond phase for Si, Ge, and Sn. Additional allotropes of Ni, C, and Sn were also investigated: body-centered cubic (bcc) Ni, diamond C, and body-centered tetragonal (bct) Sn. NiX alloys ($X = $ C, Si, Ge, and Sn) were chosen based on the alloy with the lowest alloy mixing energy reported in the Materials project database [57,58]. The structural information for all models was taken from the same database and served as the input for geometry optimization. Only one composition was investigated for NiSi and NiGe alloys, whereas for NiSn, three low-temperature alloys were considered. Table I summarizes structural parameters of the investigated single-component and binary systems used in this work.

D. Evaluated properties

1. Bulk structural parameters of the single-component elements

Bulk lattice constants of the pure elements for Ni fcc, C, Si, Ge and Sn diamond, and the interlayer spacing in C graphite were calculated and compared with experiments. The

TABLE I. Crystallographic data used as structural input in this study. For cubic lattices, only a and α are given; for hexagonal lattices, only a and c are presented.

Chemical Symbol (Phase)	Space Group	a, b, c [Å] $(\alpha, \beta$ Angles $^\circ)$	Materials Project ID	Expt. Refs.
Ni (fcc)	$Fn\bar{3}m$ (225)	2.479 (60)	mp-23	[59]
Ni (bcc)	$Im\bar{3}m$ (229)	2.416 (109)	mp-1008728	
C (graphite)	$P6_3/mmc$ (194)	2.468, 8.685 (90, 120)	mp-48	[60]
C (diamond)	$Fd\bar{3}m$ (227)	2.527 (60)	mp-66	[61]
Si (diamond)	$Fd\bar{3}m$ (227)	3.867 (60)	mp-149	[62]
Ge (diamond)	$Fd\bar{3}m$ (227)	4.075 (60)	mp-32	[63,64]
Sn (diamond)	$Fd\bar{3}m$ (227)	4.700 (60)	mp-117	[65]
Sn (bct)	$I4_1/amd$ (141)	4.482 (97, 137)	mp-84	[66]
Ni$_3$C	$R\bar{3}C$ (167)	5.051 (54)	mp-7586	
Ni$_2$Si	$Pnma$ (62)	3,734, 4.983, 7.068 (90)	mp-1118	
Ni$_5$Ge$_3$	$C2/c$ (15)	6.369 (64)	mp-1428	
Ni$_3$Sn	$P6_3/mmc$ (194)	5.305, 4.242 (90, 120)	mp-20112	[67–69]
Ni$_3$Sn$_2$	$Pnma$ (62)	5.218, 7.127, 8.208 (90)	mp-669720	[69–71]
Ni$_3$Sn$_4$	$C2/m$ (12)	6.472, 5.270, (76, 37)	mp-20174	[69]

percentage error (PE) by a functional was calculated as

$$\text{PE} = \frac{\xi_{\text{theo}} - \xi_{\text{exp}}}{\xi_{\text{exp}}}, \qquad (4)$$

where ξ_{exp} is the experimental value of the property and ξ_{theo} is its computed value.

2. Relative stability of NiX alloys

Relative stabilities were calculated per atom in the unit cell for Ni, C, Si, Ge, and Sn. The reference structures were the most stable phase/allotrope of each element: for Ni it is the fcc phase, for C it is the graphite, and for Si, Ge, and Sn it is the diamond phase.

3. Alloy mixing energy for NiX alloys

The alloy mixing energy ΔE_{mix} per atom for the NiX alloys is defined as follows:

$$\Delta E_{\text{mix}} = \frac{E(\text{Ni}_x X_y) - xE(\text{Ni}) - yE(X)}{x + y}, \qquad (5)$$

where $E(\text{Ni}_x X_y)$, $E(\text{Ni})$, and $E(X)$ are the total energies per atom of the NiX alloy, and the single-component Ni and X, respectively, and x and y are the number of atoms for Ni and X in the alloy unit cell. The single-component bulk phases are Ni fcc, C graphite, Si, Ge, and Sn diamond. ΔE_{mix} is calculated without taking into account vibrational and/or entropic effects.

E. Correlation analysis between functional steepness and bulk properties

In Ref. [37], it was observed that it is possible to obtain a linear relation between computed energetic and structural properties and the "steepness" of the enhancement factor $F_x(s)$ within each class of density functionals, e.g., GGA or vdW-DF. The steepness is defined as the value of the enhancement factor at a particular optimal reduced density gradient value, s_{opt}, which is specific for each property and functional class. This observation was used to devise a computational scheme

to improve the predictive power of density functional theory for material properties. In this work we further explore this possibility for binary systems (NiX alloys).

The steepness of $F_x(s)$ in Ref. [37] was best represented using a F_x calculated at a particular optimal s_{opt} value resulting in a maximal regression between computed properties and $F_x^{s_{\text{opt}}}$ for different density functionals. In practice, s_{opt} was found by computing $F_x(s)$ for s values ranging from 0 to 2.5 with the different density functionals (a vertical line in Fig. 1), followed by a regression analysis at each point with respect to corresponding materials properties. To maximize the regression, one s_{opt} value for each property and class of density functionals (grouped according to their level of approximation, e.g., GGA or vdW-DF) was obtained.

In this analysis, only GGA and vdW-DF functionals were considered. GGA-D3 functionals were not included because the exchange enhancement factor is the same for the parent GGA functional, and the dispersion correction applied *a posteriori* will merely cause a close to a constant shift of the fitted line. The meta-GGA functionals SCAN and SCAN-rVV10 were not included since these functionals have different exchange enhancement factors depending on the electronic kinetic energy density and the mapping of the reduced density gradient in the unit cell.

III. RESULTS AND DISCUSSION

Our previous work considered only a single-component system of Ni where trends in computed properties were rationalized based on differences in the reduced density gradient for each system (bulk, surfaces, and nanoparticles) [37]. The computed data was also used in a scheme for predicting properties where experiments are uncertain. Herein, we use the same approach for binary bulk systems in the form of NiX alloys (X = C, Si Ge, and Sn). This section starts by reporting computed material properties of single-component bulk materials from group 14, and after that, we turn to the NiX alloy systems.
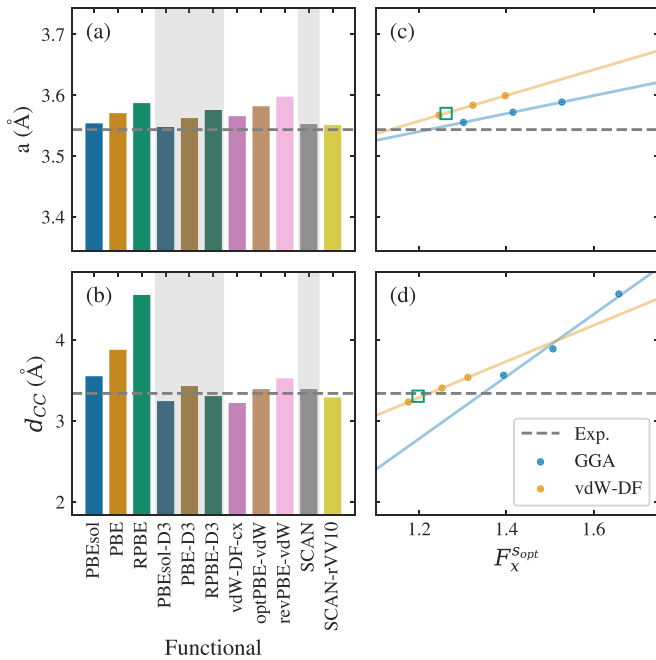
FIG. 2. Structural data calculated using GGA, GGA-D3, vdW-DF, and meta-GGA functionals for C diamond and C graphite and their regression with $F_x^{S_{opt}}$ for GGA and vdW-DF functionals. (a) Conventional lattice parameter for C diamond, (b) interlayer distance of C graphite, (c) linear regression between $F_x^{S_{opt}}$ and lattice parameter for C diamond, and (d) linear regression between $F_x^{S_{opt}}$ and interlayer distance for C graphite. The square marker is the computed property with the optB86b-vdW functional and its corresponding $F_x^{S_{opt}}$ (see Sec. III C for details).

A. Structural properties of bulk structures from group 14

We start discussing the diamond phase, focusing only on C but similar trends were also obtained for Si, Ge, and Sn. For comparison, lattice parameters and the percentage errors for all structures can be found in the Supplemental Material [72]. In the following, we will discuss structural properties followed by energetics. After the discussion of each property, we discuss the regression analysis.

In Fig. 2(a), we show the lattice constants computed using different density functionals. All functionals are found to describe the lattice constant for C diamond with good accuracy ($0.17\% \leqslant PE \leqslant 1.57\%$, the least accurate being revPBE-vdW), although all functionals overestimate the lattice, which is a common feature of GGAs [20,73]. Among the GGA functionals, the one optimized for condensed phase systems (PBEsol) is closer to the experimental value (PE = 0.33%). The inclusion of Grimme's D3 dispersion correction shrinks the cell, thus making PBEsol-D3 the most accurate among all investigated functionals here, with PE = 0.17%. Similarly to the GGA functionals, all vdW-DF functionals overestimate the lattice constant (PE is 0.67%, 1.13%, and 1.57% for vdW-DF-cx, optPBE-vdW, and revPBE-vdW, respectively), following the same trend as for GGA functionals with respect to the functional character in terms of "steepness" in the enhancement factor $F_x(s)$ as discussed above (cf. Fig. 1). For the meta-GGA SCAN, the computed lattice constant is off by only 0.30% and the inclusion of long-range dispersion

correction through the rVV10 formalism has a small effect on the lattice parameter (SCAN-rVV10 PE = 0.26%).

Next, we move on to C graphite, a typical example of a material where dispersion interactions play a critical role in dictating the interlayer distance, and it is known that the correct description by DFT is only achieved when dispersion corrections are included [74–76]. Figure 2(b) shows the calculated interlayer distance for graphite using different functionals and different dispersion corrections.

For the GGA functionals, the more "molecular oriented" the functional is, i.e., having a higher $F_x(s)$ steepness, the less accurate it becomes (PE going from 6.70% for PBEsol to 36.75% for RPBE). Employing the *a posteriori* dispersion correction through Grimme's D3 approach greatly improves the interlayer distance [the PE for GGA-D3 functionals lies between -2.49% (PBEsol-D3) and 3.08% (PBE)]. Moreover, the RPBE prediction goes from a severe overestimation to a very accurate prediction of the interlayer distance when including D3 corrections (PE = -0.63% for RPBE-D3). The self-consistent dispersion corrected functionals (vdW-DF class) generally show good performance when describing structural parameters of graphite. The interlayer distance is slightly underestimated using vdW-DF-cx (PE = -3.19%) and slightly overestimated for optPBE-vdW and revPBE-vdW (PE = 1.96% and 5.91%, respectively). The meta-GGA density functional SCAN (PE = 2.04%) gives similar results as optPBE-vdW. The inclusion of dispersion in SCAN-rVV10 shrinks the interlayer distance making SCAN-rVV10 to have PE = -1.12%. Interestingly, while the variations in the predicted interlayer spacing are considerable for the GGA functionals, the addition of dispersion corrections, either using an *a posteriori* or vdW-DF approach, brings the variation among different predictions to similar percentages as found for the diamond structure.

Now let us apply the regression model for the lattice of C diamond and the interlayer distance of C graphite. As discussed in Ref. [37], different classes of functionals, with and without van der Waals corrections, will provide a different linear $F_x^{S_{opt}}$ dependence. Therefore, we perform the regression analysis for the two classes (GGA and vdW-DF) separately, cf. Fig. 2(c). As expected, we observe a clear linear relationship between the $F_x^{S_{opt}}$ and the lattice parameter for both the GGA and vdW-DF functionals. At a certain $F_x^{S_{opt}}$ value both functionals will give an accurate prediction of the lattice constant. An accurate prediction of the lattice constant within the vdW-DF occurs for a lower $F_x^{S_{opt}}$ value compared to the GGA class, but since C diamond is mainly covalently bonded, the difference is not so significant.

Figure 2(d) shows the regression for the interlayer distance between C layers in graphite and $F_x^{S_{opt}}$ for GGA and vdW-DF functionals. Here, we observe larger differences in the resulting regressions for the two density functional classes compared to the regressions in Fig. 2(c) for C diamond. For the interlayer distance, the regression for GGA is not as good as for vdW-DF (the correlation between $F_x^{S_{opt}}$ and d_{CC} is more scattered for GGA, blue dots), indicating that exchange alone is not sufficient to describe the interlayer distance accurately. Although the regression for the GGA class will eventually cross the experimental dashed line, the correct lattice constant will, in this case, be obtained for the wrong reasons.
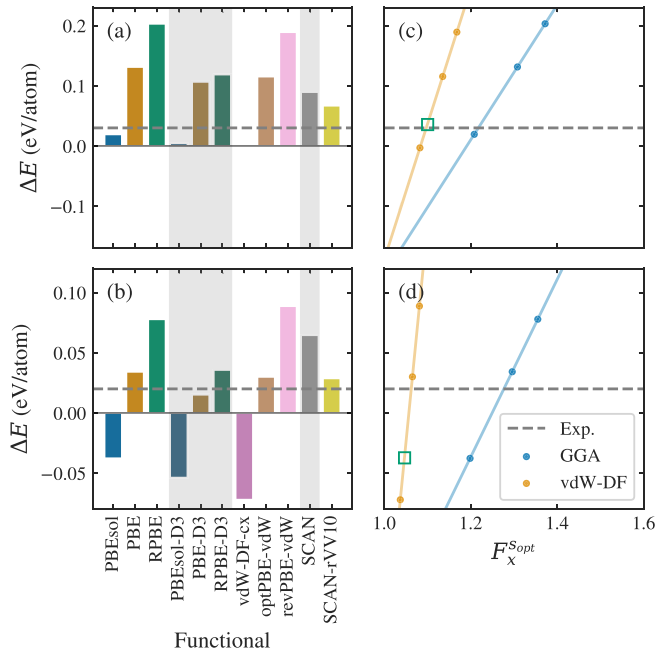
FIG. 3. The relative stability (ΔE) per atom for C and Sn allotropes was calculated using GGA, GGA-D3, vdW-DF, and meta-GGA functionals. (a) is ΔE of C diamond with respect to C graphite, and (b) is ΔE of Sn diamond with respect to bct. (c) and (d) are the GGA and vdW-DF linear regression models between $F_x^{s_{opt}}$ and ΔE for C and Sn, respectively. The square marker is the computed property with the optB86b-vdW functional and the corresponding $F_x^{s_{opt}}$ (see Sec. III C for details).

Compensating the lack of nonlocal correlation with exchange to predict one property accurately will most certainly affect the possibility to predict other properties accurately.

B. Relative stabilities of carbon and tin allotropes

Alloy stabilities are typically referenced to the energetics of the corresponding single-component systems. Calculating such properties with DFT is often challenging since the nature of the chemical bonds in alloys may change upon mixing. In the NiX alloy systems studied here, we have Ni, a metal, mixed with X, a semiconductor. In the following, we first investigate how different density functional approximations perform on allotropes of the pure elements. We focus on total energy differences rather than atomization energies to circumvent the problem in DFT in calculating reference atomic energies [37,41].

Figure 3(a) shows the relative stability per atom of the two C allotropes discussed above (diamond and graphite). Positive numbers infer that graphite is more stable than diamond. Experimentally, graphite is well known to be the most stable polymorph at normal conditions (1 atm and 298 K). Using the various density functionals presented above, we note that the energy difference between these allotropes can be as large as 0.20 eV/atom (RPBE). Here, PBEsol and SCAN-rVV10 are functionals that give a total energy difference closest to the experimental value of 0.02 eV/atom [77,78]. For the GGA class of density functionals, having a functional with a slower "steepness" in $F_x(s)$, i.e., tuned towards an accurate

description of the condensed phase, brings the result closer to experimental observations. Hence, PBEsol is the GGA functional that gives an accurate description of relative stabilities. On the contrary, as observed for the interlayer distance in C graphite, adding Grimme's D3 dispersion correction only slightly affects the relative stability between the two C allotropes, resulting in an overestimation of the diamond stability for PBE-D3 and RPBE-D3. For the vdW-DF functionals, vdW-DF-cx predicts that C graphite is as stable as C diamond. In contrast, optPBE-vdW and revPBE-vdW follow the overall trend for the GGA functionals, i.e., an overestimation of the relative energy. For the meta-GGA functionals, the inclusion of dispersion in SCAN-rVV10 slightly improves the agreement with experimental observations.

Next, we move on to the relative stability of the two most stable Sn allotropes. From experiments, these are the diamond phase (α-Sn), stable at low temperatures ($T < 13\,^{\circ}$C), and a bct phase (β-Sn), stable at higher temperatures. The relative energy difference between these Sn allotropes at 0 K is only 0.02 eV/atom [79,80], and as for the C relative energies discussed above, an accurate prediction using DFT for this slight energy difference is a challenge. Let us see how the studied functionals herein perform.

The computed relative energies are given in Fig. 3(b). Compared to the C results, we observe more drastic errors in predicting which phase is stable at 0 K. For the GGA functionals, the PBE functional predicts the expected energy difference between the Sn allotropes. In contrast, the PBEsol functional overestimates the stabilization of the bct phase, and the RPBE functional overestimates the stability of the diamond phase. The inclusion of Grimme's D3 vdW correction results in a slight stabilization of the bct phase, thus making PBE-D3 the most accurate functional here. Interestingly, the inclusion of self-consistent dispersion corrections does not improve the relative energies for the Sn allotropes. The vdW-DF-cx functional overestimates the stabilization of the bct phase while the optPBE-vdW and revPBE-vdW functionals stabilize the diamond phase. As for SCAN and SCAN-rVV10, both functionals overestimate the diamond phase stability, although the inclusion of dispersion corrections in SCAN-rVV10 considerably improves the results.

The results obtained when applying PBEsol, PBEsol-D3, or vdW-DF-cx functionals indicate that a phase transformation from Sn diamond (α-Sn) to Sn bct (β-Sn) would never occur since the bct phase will always be more stable than the Sn diamond. Such a wrong prediction of phases stabilities may have consequences on *ab initio* phase diagrams and on the conclusions drawn from thermodynamic calculations using for example the CALPHAD method. Compared to the case for C allotropes, the diamond phase was at least as stable as graphite, even though the relative energy was overestimated in some cases. Therefore, we emphasize the importance of carefully validating results from DFT calculations before using them in multiscale modelling approaches.

As for structural properties, one can make a linear regression model for the relative stabilities of C and Sn to investigate trends among the results. We again observe for C relative stabilities, cf. Fig. 3(c), that the regression for vdW-DF crosses the experimental value at smaller $F_x^{s_{opt}}$ compared to the regression for GGA functionals, although the difference is not
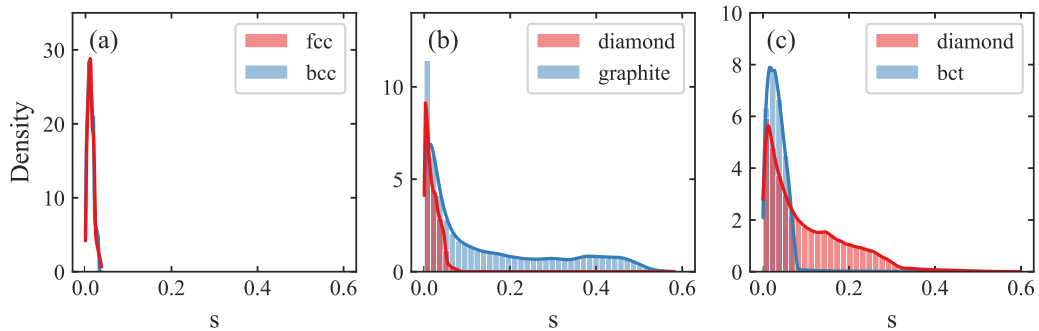
FIG. 4. Reduced density gradient distributions for (a) Ni fcc (red) and bcc (blue) phases, (b) C diamond (red) and graphite (blue), and (c) Sn diamond (red) and bct (blue) phases.

as large as for the regression for the interlayer distance. Even though dispersion corrections are important for the interlayer distance in graphite, it is important to highlight that the main contribution for an accurate description of C relative stabilities arises from the exchange since covalent bonds between the atoms are the main contribution to the total energies. The same conclusions drawn for C are valid for the computed Sn relative stabilities, cf. Fig. 3(d). However, the slope of the regressions for the relative stabilities of Sn allotropes shows that a slight change in how the exchange is computed causes a substantial effect in the calculated property, especially for the vdW-DF class.

C. Validation of regression model and further explorations of $F_x^{S_{opt}}$

In Secs. III A and III B we have shown that it is possible to find a $F_x^{S_{opt}}$ value that coincides with the experimental value of a given materials property. In Ref. [37], this observation was used to derive a scheme for predicting properties where experiments are uncertain or even lacking. One problem with this scheme is that the lack of experimental data makes validation difficult. In this section, we therefore propose another means of validation by predicting the results of other density functionals using the already fitted regression model $F_x^{S_{opt}}$. For this purpose, we have chosen to use the density functional optB86b-vdW, which has previously been shown to be very accurate in predicting structural properties of molecules and materials [81]. The $F_x^{S_{opt}}$ values and the corresponding computed material property calculated using the optB86b-vdW functional are indicated by the green squares in Figs. 2(c) and 2(d) and Figs. 3(c) and 3(d). As seen in the figures, the computed values lie very close to the estimated values given by the linear regression. This exercise demonstrates the robustness of the approach taken and provides further support for the proposed extrapolation scheme for improved predictability of materials properties with DFT.

D. Reduced density gradient distributions of Ni, C, and Sn allotropes

Now let us put the results shown for C and Sn allotropes into the perspective of finding a suitable functional for describing the single-component elements of an alloy. For Ni, we observed a negligible difference among the functionals

for the relative energy between the fcc and bcc phase, and all predicted fcc as the stable phase [37]. On the other hand, the energy difference is ± 0.1 eV/atom for C allotropes, and the difference for Sn allotropes is ± 0.08 eV/atom. One can understand the results obtained when using different functionals for Ni, C, and Sn by analyzing each allotrope's reduced density gradient distribution. We observe in Fig. 4(a) that both Ni fcc and bcc have a very similar distribution of reduced density gradients, while the distribution for graphite shows a wider spread compared to the distribution for diamond, cf. Fig. 4(b) blue and red bins, respectively. For small s values, as for fcc, bcc, and diamond, all functionals will produce similar results, since $F_x(s) \approx 1$ when $s \approx 0$. On the other hand, the wider spread in s values for graphite will affect how the exchange energy is computed for each functional, leading to a larger span in the computed property values.

Looking at the reduced density gradient distribution of Sn diamond and bct, Fig. 4(c), we also observe less overlap between the two distributions than for Ni fcc and bcc. However, the spread in s values is not as large as for C graphite, which could explain why the span in computed energy differences in Sn allotropes is less than for the C allotropes. One could also say that the different contributions to the exchange energy for the Sn diamond phase contribute the most to the different results for relative stabilities. By looking at $F_x(s)$ for GGA and vdW-DF functionals, one sees that the weak dependence of PBEsol and vdW-DF-cx tend to overstabilize the metallic (bct) phase due to a "penalty" of the exchange energy in Sn diamond. On the contrary, for PBE, RPBE, optPBE-vdW, and revPBE-vdW, the $F_x(s)$ tend to stabilize systems with a higher contribution from the exchange at larger s values, and therefore, the diamond phase is favored. Finally, the flexibility in SCAN when treating various chemical bonds, as discussed in Sec. II, tends to favor the diamond phase, and the inclusion of nonlocal correlation improves the description of relative stabilities.

To conclude the discussion on single-component elements of group 14, we observe that the relative stabilities of C allotropes are accurately achieved by an accurate description of exchange, which can be obtained by analyzing the value of $F_x^{S_{opt}}$ when the regression model crosses the experimental value. However, dispersion interactions are crucial for describing the interlayer distance in graphite. We note that for relative stabilities of C and Sn allotropes, there is a delicate balance on how much the exchange energy should
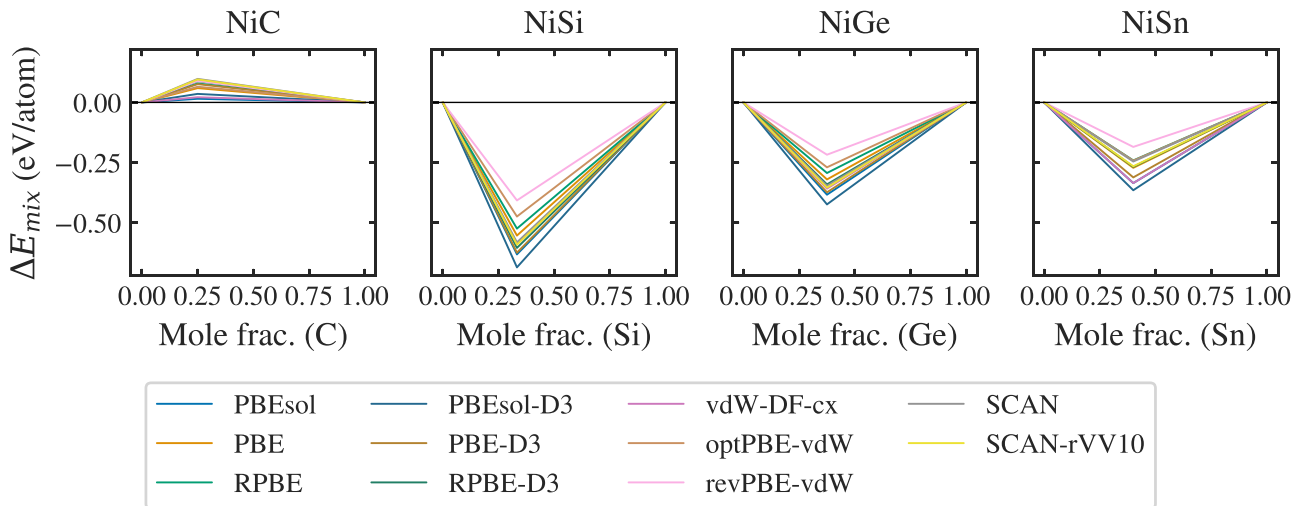
FIG. 5. Alloy mixing energies (ΔE_{mix}) for NiX alloys (X = C, Si, Ge, Sn) calculated using GGA, GGA-D3, vdW-DF, and meta-GGA functionals.

be accounted for in order to produce accurate results. The discussions from the regression model reinforce that a GGA or vdW-DF functional can either be accurate for structural parameters or relative energies but never both. However, an accurate description of exchange is crucial for the transferability of the functional. Our results show that the meta-GGA formalism indeed solves some of these problems and is transferable over a wider variety of chemical bonding situations.

E. Properties of *NiX* alloys

The next step in this work is to investigate how the choice of density functional affects the prediction of specific alloy bulk properties. Besides C, which has been found to form interstitial alloys with Ni, all other group 14 elements form stable substitutional alloys [69,82,83]. Due to the increased complexity in studying interstitial alloys, we have focused only on substitutional ones in this work. We have chosen the following set of substitutional alloys: Ni$_3$C, Ni$_2$Si, Ni$_5$Ge$_3$, and Ni$_3$Sn$_4$. Among these, the nickel carbide is not stable under standard conditions [84,85] but is still interesting in the purpose of testing density functionals. Information about the structures can be found in Sec. II C, in Table I, and in the Supplemental Material [72].

Starting with structural properties, we observe the same trend for the alloys as for the single-component systems (lattice parameters for all investigated alloys are found in the Supplemental Material [72]). PBEsol (RPBE) gives the smallest (largest) lattice parameter among GGAs, the inclusion of D3 corrections shrinks the cell, and vdW-DF functionals follow the same trend as GGA class when it comes to functional steepness: vdW-dDF-cx gives the smallest and revPBE-vdW the largest lattice parameter. Finally, the inclusion of dispersion corrections in SCAN-rVV10 does not significantly affect the computed lattice parameters. Note that it is not possible to evaluate which functional that predicts the best structural properties since, to the best of our knowledge, experimental lattice constants extrapolated to 0 K are not available in the literature for the systems investigated in this work.

Next, we evaluate the stability of NiX alloys by calculating ΔE_{mix} according to Eq. (5) for each alloy and for each functional. These results are reported in Fig. 5. For Ni$_3$C, all functionals correctly predict that this alloy is not stable (positive ΔE_{mix} values). For the Ni$_2$Si, Ni$_5$Ge$_3$, and Ni$_3$Sn$_4$ alloys, all functionals predict that they are stable (negative ΔE_{mix} values). We note that even though the different functionals predict a wide span of mixing energies, one can conclude that all of them are in qualitative agreement when it comes to predicting the stability (the sign of ΔE_{mix}) of NiX alloys.

Let us look a little closer at the data for the stable NiSi, NiGe, and NiSn alloys in Fig. 5 (see also Supplemental Material [72]). We note that for all alloys, the revPBE-vdW functional gives the smallest absolute value of ΔE_{mix} (least stable), whereas PBEsol-D3 gives the largest (most stable). The energy spread in computed ΔE_{mix} decreases going down the group 14: 0.28, 0.21, and 0.19 eV/atom, respectively, for Ni$_2$Si, Ni$_5$Ge$_3$, and Ni$_3$Sn$_4$. Grimme's D3 dispersion correction always decreases the absolute ΔE_{mix} value (makes it less stable), but for the meta-GGA SCAN functional, the self-consistent dispersion correction in the form of rVV10 kernel has little effect on computed ΔE_{mix} values.

At this point, there are, to the best of our knowledge, no experimental data to validate the computed ΔE_{mix} against, which makes it difficult to judge which is the most accurate functional for a quantitative prediction of the computed ΔE_{mix}. We note, however, a large spread in computed mixing energies, which of course, will affect the phase diagram of the respective alloys. We only discuss the mixing energies computed at 0 K here and do not aim to calculate the actual transition temperatures, which would require the computation of entropic effects upon the phase transformation and alloy formation. However, if we assume that the calculation of ΔE_{mix} causes similar consequences for the phase transformation as we discussed for the diamond-to-bct phase transformation of Sn in Section III B, it is clear that different functionals will predict different phase transition temperatures. In the following section, we will demonstrate how our regression analysis can deal with these problems.
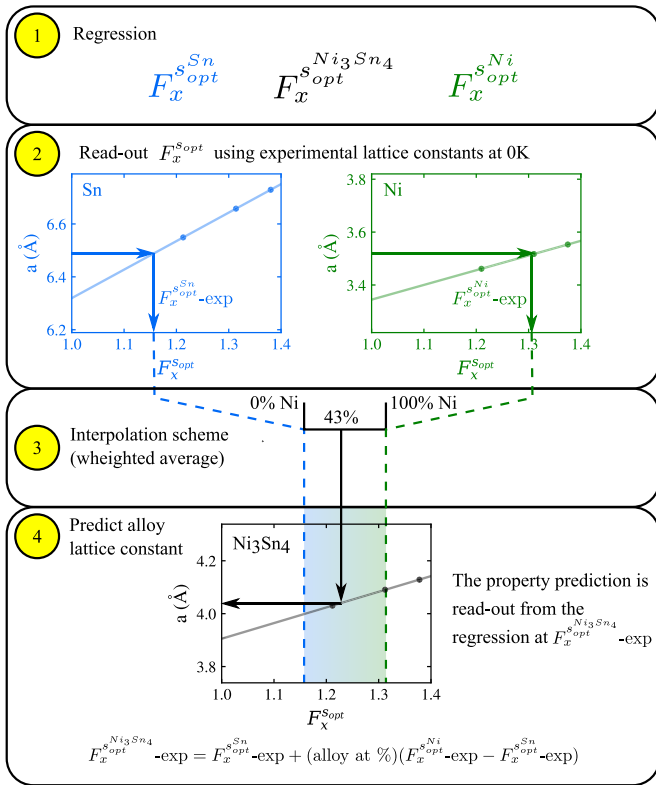
FIG. 6. Schematic representation for predicting the experimental value of the lattice constant in the Ni_3Sn_4 alloy (see text for a detailed explanation).

F. Lattice constants and ΔE_{mix} for NiSn alloys with various compositions

Since there only exists sparse experimental data for alloys in the scientific literature, it is not easy to judge which functional best describes multicomponent systems with various compositions, especially if the nature of chemical bonding in

the pure compounds of the constituents are very different. To overcome this problem, we will in the following make use of and extend our scheme for improved predictions of material properties presented in Ref. [37] to enable prediction of properties for alloys with varying composition. As discussed above, we observe a clear trend between the "steepness" of $F_x(s)$ and a computed specific property of the single-element compounds, and that the experimental value of this property can be found at a specific $F_x^{S_{opt}}$ value for single-component systems. In the extended scheme, these $F_x^{S_{opt}}$ values will serve as boundaries when predicting properties for the alloy. To demonstrate the scheme, we will in the following predict the lattice constant of Ni_3Sn_4. The procedure (also illustrated in Fig. 6) is as follows:

(i) Generate the regression model for the two single-component systems and for the alloy for a given functional class and property (in this illustration the GGA class and the lattice parameter of Ni, Sn, and Ni_3Sn_4).

(ii) Read out $F_x^{S_{opt}}$ for the experimental value of the property in the regression model for the single-component systems. We call this value $F_x^{S_{opt}}$-exp.

(iii) Interpolate $F_x^{S_{opt}}$ for the alloys according to their composition, i.e., the amount of Sn in the alloy. For example, Ni_3Sn_4 has 57 atom-% of Sn, and therefore its $F_x^{S_{opt}}$ cross is weighted averaged to 0.43 atom-% of Ni. The $F_x^{S_{opt}}$ values of the single-component systems are boundaries in the interpolation scheme.

(iv) Project the interpolated $F_x^{S_{opt}}$-exp to the regression model for the alloy and read out the predicted lattice constant.

A note on step (iii): We use an interpolation for the $F_x^{S_{opt}}$-exp of the alloy since we observed a gradual change in the s distribution following the alloy composition from Ni to Sn (see Fig. S1 in the Supplemental Material).

Now let us use this procedure to compute lattice constants for different NiSn alloys. Figure 7 shows the predicted lattice constants for Ni_3Sn, Ni_3Sn_2, and Ni_3Sn_4 together with optimized lattice constants from all considered density func-
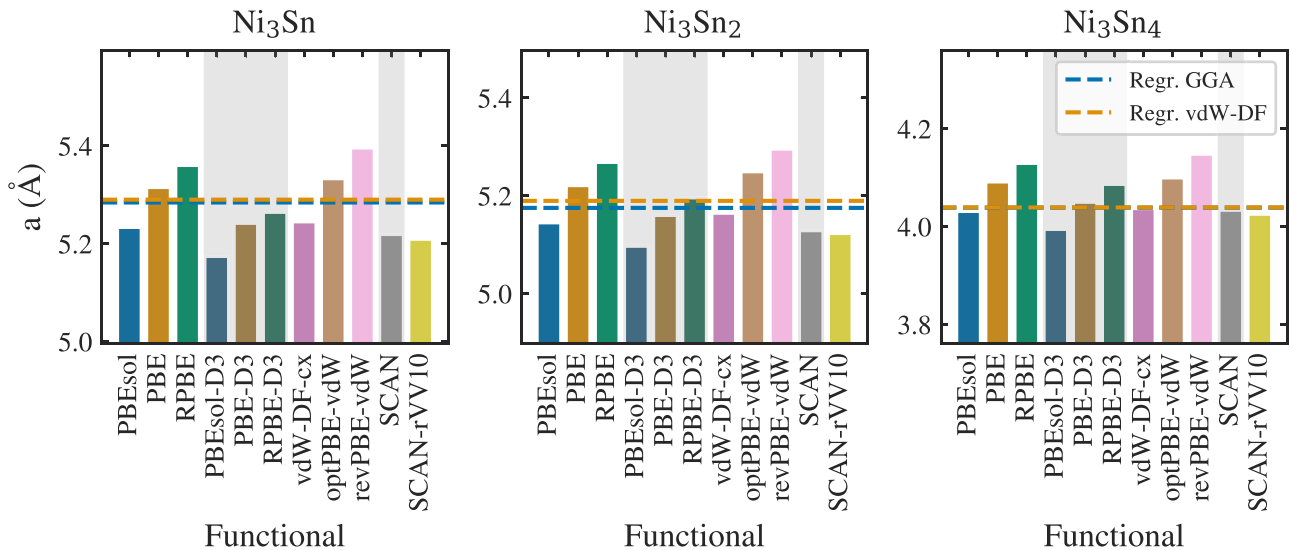

FIG. 7. Lattice parameters were calculated using GGA, GGA-D3, vdW-DF, and meta-GGA functionals for NiSn alloys with various compositions. The dashed blue and orange lines are the predicted lattice constants at $F_x^{S_{opt}}$-exp of the extended linear regression model for GGA and vdW-DF functionals, respectively.
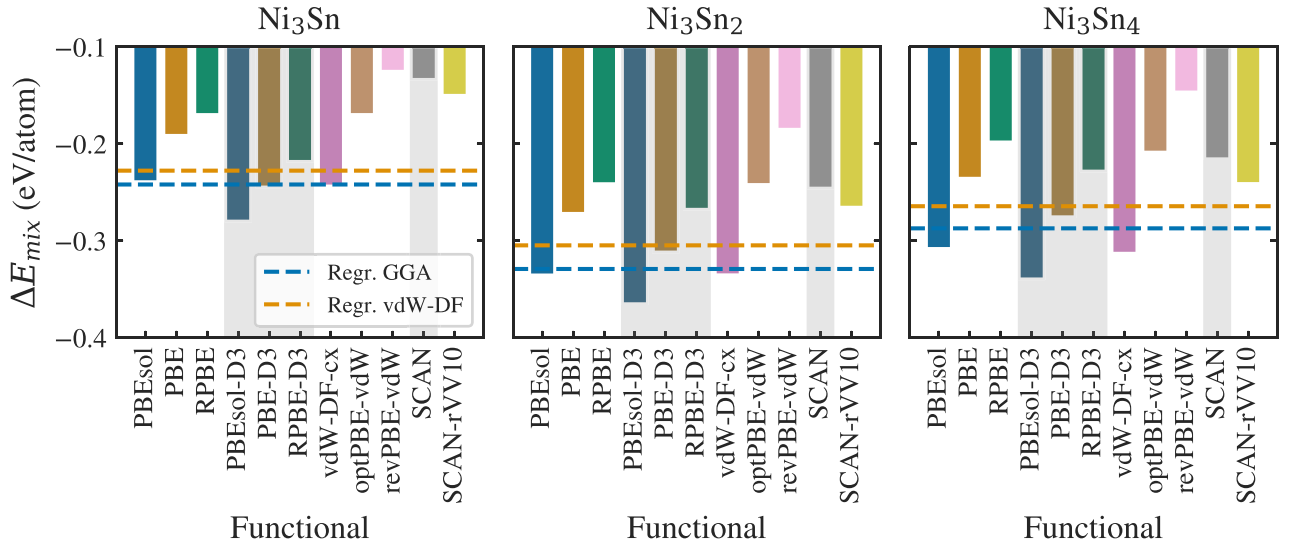
FIG. 8. ΔE_{mix} calculated using GGA, GGA-D3, vdW-DF, and meta-GGA functionals for NiSn alloys with various compositions. The dashed blue and orange lines are the predicted ΔE_{mix} at $F_x^{s_{opt}}$ cross of the linear regression for GGA and vdW-DF functionals, respectively.

tionals. In the figure, we see that the predictions made from the GGA and vdW-DF based regression models agrees to a large extent for all considered alloys. Using the predicted lattice parameters from our regression, we can now assess the quality of the different functionals. We observe that PBE and optPBE-vdW are the functionals that better describe the lattice of Ni_3Sn, and PBEsol and vdW-DF-cx the lattice of Ni_3Sn_2 and Ni_3Sn_4. RPBE and revPBE-vdW have the largest overestimation compared to the predicted lattice parameter from the regression model, suggesting that structural properties of NiSn alloys might not be well described by these functionals. The shrinkage caused by D3 dispersion corrections makes the prediction of structural parameters worse for Ni_3Sn and Ni_3Sn_2, but PBE-D3 is very good for Ni_3Sn_4. The SCAN meta-GGA functional seem to underestimate the lattice constants of Ni_3Sn and Ni_3Sn_2 but describe the structure of Ni_3Sn_4 reasonably well.

We now apply the same procedure for ΔE_{mix} of NiSn alloys. These results are reported in Fig. 8. In the case of structural parameters, it was possible to use the same property (lattice constant) to find $F_x^{s_{opt}}$-exp for the single-component systems, but ΔE_{mix} is by construction zero for Ni fcc and Sn diamond. Therefore, it is necessary to choose another property that is based on total energies. In this work, we chose the Ni(111) surface formation energy and the Sn relative stabilities for the single-component systems. These choices are motivated based on the predicted Wulff constructions for Ni nanoparticles in Ref. [37] and the discussion of Sn allotropes in Sec. III B.

Among the GGA functionals, we observe that ΔE_{mix} for PBEsol is the closest to the predicted ΔE_{mix}. The shift towards overstabilization by the D3 corrections seen in all binary systems studied here caused PBEsol-D3 to overstabilize ΔE_{mix}, and therefore PBEsol-D3 becomes less accurate. The span of results for vdW-DF functionals is larger than GGA functionals, where vdW-DF-cx tends to slightly overstabilize the alloy, whereas optPBE-vdW and revPBE-vdW tend to severely understabilize it. For the meta-

GGA functionals, an understabilization is observed for all compositions.

Finally, we conclude that it is possible to obtain a qualitative agreement among different functionals for various properties of binary systems, but the results can be quantitatively quite different. Given the difficulty in comparing the results for binary (and multicomponent) systems with experiments, the regression analysis, extensively discussed for the single-component systems above and in Ref. [37], is here proposed to be a valuable tool for rationalizing results from the various density functionals. Furthermore, it makes it possible to provide an educated guess of the accuracy of computed properties. From the theoretical side, these results can guide the development of more accurate functionals.

IV. CONCLUSIONS

We have investigated and compared the performance of different semilocal GGA and meta-GGA density functionals with and without dispersion interactions in terms of their ability to describe key properties of bulk elements of group 14 and some substitutional NiX ($X = $ C, Si, Ge, Sn) alloys.

We find for the single-component systems that the best agreements with experiments are:

(i) RPBE-D3 for C graphite interlayer distance.

(ii) PBEsol-D3 for the C and Sn diamond lattice parameters.

(iii) SCAN-rVV10 for the Si and Ge diamond lattice parameters.

(iv) PBEsol for the relative stability of C diamond with respect to graphite.

(v) PBE, optPBE-vdW, and SCAN-rVV10 for the relative stability of Sn bct with respect to Sn diamond.

These results suggest that the quantitative performance of a density functional is system and property dependent. Therefore, none of the functionals studied here can simultaneously describe all the different chemical characteristics that can be found in materials based on the elements from group 14.

We further rationalized our results in the light of a regression model that correlates a specific property with the steepness of the exchange enhancement factor $F_x(s)$ for a given class of density functionals, e.g., GGA or vdW-DF, obtained by maximizing the regression at a certain s_{opt} value. For the single-component systems, we show that it is possible to capture the experimental value (or theoretical) for certain properties using the generated regression model for $F_x^{s_{opt}}$.

We also investigated how the choice of density functional affects the prediction of key properties in binary NiX alloys. We observed that all functionals qualitatively agree on the stability of the alloys. However, quantitatively, the computed data is scattered, both in terms of their predicted lattice parameters and ΔE_{mix}. Regarding their predicted structural and energetic properties, we observed that they follow the same trend as the single-component systems concerning the steepness of the exchange enhancement factor. Based on this observation, we extended the scheme for improved property prediction in DFT presented in Ref. [37] to binary compounds. We foresee that the use of regression models (or extensions of such) can be valuable in the development of more accurate density functionals that in the future could provide quantitative accuracy even for complex multicomponent systems.

[1] M. Lindholm and B. Sundman, A thermodynamic evaluation of the nickel-silicon system, Metallurgical and Materials Transactions A **27**, 2897 (1996).

[2] P. A. Nikolaychuk and A. G. Tyurin, Thermodynamic assessment of chemical and electrochemical stability of nickel–silicon system alloys, Corrosion Sci. **73**, 237 (2013).

[3] L. Lajaunie, M. David, F. Pailloux, C. Tromas, E. Simoen, C. Claeys, and J. Barbot, Influence of the pre-treatment anneal on co–germanide schottky contacts, Mater. Sci. Semicond. Proc. **11**, 300 (2008).

[4] Y. Deng, O. Nakatsuka, J. Yokoi, N. Taoka, and S. Zaima, Epitaxial formation and electrical properties of Ni germanide/Ge(110) contacts, Thin Solid Films **557**, 84 (2014).

[5] Y. Liu, J. Xu, J. Liu, G. Wang, X. Luo, D. Zhang, S. Mao, Y. Li, J. Li, C. Zhao, W. Wang, B. Gao, D. Chen, T. Ye, and J. Luo, Role of carbon pre-germanidation implantation on enhancing the thermal stability of NiGe films below 10 nm thickness, ECS J. Solid State Sci. Techn. **9**, 054006 (2020).

[6] Y. Zhang, Tin and tin alloys for lead-free solder, in *Modern Electroplating* (John Wiley & Sons, Inc., New Jersey, 2011), pp. 139–204.

[7] S. Amares and B. Tchari, Effect on shear strength and hardness properties of tin based solder alloy, Sn-50Bi, Sn-50Bi + 2%TiO$_2$ nanoparticles, Adv. Mater. Res. **1159**, 54 (2020).

[8] M. Zienkiewicz-Machnik, I. Goszewska, A. Śrębowata, A. Kubas, D. Giziński, G. Słowik, K. Matus, D. Lisovytskiy, M. Pisarek, and J. Sá, Tuning nano-nickel selectivity with tin in flow hydrogenation of 6-methyl-5-hepten-2-one by surface organometallic chemistry modification, Catalysis Today **308**, 38 (2018).

[9] F. de Assis Rocha da Silva, R. C. R. dos Santos, R. S. Nunes, and A. Valentini, Role of tin on the electronic properties of Ni/Al$_2$O$_3$ catalyst and its effect over the methane dry reforming reaction, Applied Catalysis A: General **618**, 118129 (2021).

[10] M. Klarner, S. Bieger, M. Drechsler, and R. Kempe, Chemoselective hydrogenation of olefins using a nanostructured nickel catalyst, Zeitschrift für anorganische und allgemeine Chemie **647**, 2157 (2021).

[11] A. van de Walle, M. Asta, and G. Ceder, The alloy theoretic automated toolkit: A user guide, Calphad **26**, 539 (2002).

[12] A. Walle and G. Ceder, Automating first-principles phase diagram calculations, J. Phase Equilib. **23**, 348 (2002).

[13] D. D. Fontaine, Cluster approach to order-disorder transformations in alloys, in *Solid State Physics* (Elsevier, Massachusetts, 1994), pp. 33–176.

[14] M. I. Baskes, Modified embedded-atom potentials for cubic materials and impurities, Phys. Rev. B **46**, 2727 (1992).

[15] M. I. Baskes and R. A. Johnson, Modified embedded atom potentials for HCP metals, Modell. Simul. Mater. Sci. Eng. **2**, 147 (1994).

[16] B.-J. Lee and M. I. Baskes, Second nearest-neighbor modified embedded-atom-method potential, Phys. Rev. B **62**, 8564 (2000).

[17] B.-J. Lee, M. I. Baskes, H. Kim, and Y. K. Cho, Second nearest-neighbor modified embedded atom method potentials for bcc transition metals, Phys. Rev. B **64**, 184102 (2001).

[18] L. Kaufman, P. Rudman, J. Stringer, and R. Jaffee, Phase stability in metals and alloys, edited by P. S. Rudman and I. Stringer (McGraw-Hill, New York, 1967).

[19] P. Spencer, A brief history of CALPHAD, Calphad **32**, 1 (2008).

[20] P. Janthon, S. A. Luo, S. M. Kozlov, F. Viñes, J. Limtrakul, D. G. Truhlar, and F. Illas, Bulk properties of transition metals: A challenge for the design of universal density functionals, J. Chem. Theory Comput. **10**, 3832 (2014).

[21] J. P. Perdew, Jacob's ladder of density functional approximations for the exchange-correlation energy, in AIP Conference Proceedings (AIP, Antwerp, 2001).

[22] J. Klimeš and A. Michaelides, Perspective: Advances and challenges in treating van der Waals dispersion forces in density functional theory, J. Chem. Phys. **137**, 120901 (2012).

[23] P. Hohenberg and W. Kohn, Inhomogeneous electron gas, Phys. Rev. **136**, B864 (1964).

[24] G. P. Chen, V. K. Voora, M. M. Agee, S. G. Balasubramani, and F. Furche, Random-phase approximation methods, Annu. Rev. Phys. Chem. **68**, 421 (2017).

[25] S. Grimme, Accurate description of van der Waals complexes by density functional theory including empirical corrections, J. Comput. Chem. **25**, 1463 (2004).

[26] S. Grimme, Semiempirical GGA-type density functional constructed with a long-range dispersion correction, J. Comput. Chem. **27**, 1787 (2006).

[27] S. Grimme, J. Antony, S. Ehrlich, and H. Krieg, A consistent and accurate *ab initio* parametrization of density functional dispersion correction (DFT-D) for the 94 elements H-pu, J. Chem. Phys. **132**, 154104 (2010).

[28] M. Dion, H. Rydberg, E. Schröder, D. C. Langreth, and B. I. Lundqvist, Van der Waals Density Functional for General Geometries, Phys. Rev. Lett. **92**, 246401 (2004).

[29] T. Thonhauser, V. R. Cooper, S. Li, A. Puzder, P. Hyldgaard, and D. C. Langreth, Van der Waals density functional: Self-consistent potential and the nature of the van der Waals bond, Phys. Rev. B **76**, 125112 (2007).

[30] F. Furche and T. V. Voorhis, Fluctuation-dissipation theorem density-functional theory, J. Chem. Phys. **122**, 164106 (2005).

[31] O. A. von Lilienfeld and A. Tkatchenko, Two- and three-body interatomic dispersion energy contributions to binding in molecules and solids, J. Chem. Phys. **132**, 234109 (2010).

[32] J. G. Ángyán, R.-F. Liu, J. Toulouse, and G. Jansen, Correlation energy expressions from the adiabatic-connection fluctuation–dissipation theorem approach, J. Chem. Theory Comput. **7**, 3116 (2011).

[33] É. D. Murray, K. Lee, and D. C. Langreth, Investigation of exchange energy density functional accuracy for interacting molecules, J. Chem. Theory Comput. **5**, 2754 (2009).

[34] R. A. Boto, J. Contreras-García, J. Tierny, and J.-P. Piquemal, Interpretation of the reduced density gradient, Mol. Phys. **114**, 1406 (2015).

[35] E. Pastorczak and C. Corminboeuf, Perspective: Found in translation: Quantum chemical tools for grasping non-covalent interactions, J. Chem. Phys. **146**, 120901 (2017).

[36] T. Jenkins, K. Berland, and T. Thonhauser, Reduced-gradient analysis of van der Waals complexes, Electron. Struct. **3**, 034009 (2021).

[37] A. M. de Andrade, J. Kullgren, and P. Broqvist, Quantitative and qualitative performance of density functional theory rationalized by reduced density gradient distributions, Phys. Rev. B **102**, 075115 (2020).

[38] E. H. Lieb and S. Oxford, Improved lower bound on the indirect coulomb energy, Int. J. Quantum Chem. **19**, 427 (1981).

[39] J. P. Perdew, K. Burke, and M. Ernzerhof, Generalized Gradient Approximation Made Simple, Phys. Rev. Lett. **77**, 3865 (1996).

[40] J. P. Perdew, K. Burke, and M. Ernzerhof, Generalized Gradient Approximation Made Simple [Phys. Rev. Lett. **77**, 3865, (1996)] Phys. Rev. Lett. **78**, 1396 (1997).

[41] J. P. Perdew, A. Ruzsinszky, G. I. Csonka, O. A. Vydrov, G. E. Scuseria, L. A. Constantin, X. Zhou, and K. Burke, Restoring the Density-Gradient Expansion for Exchange in Solids and Surfaces, Phys. Rev. Lett. **100**, 136406 (2008).

[42] B. Hammer, L. B. Hansen, and J. K. Nørskov, Improved adsorption energetics within density-functional theory using revised perdew-burke-ernzerhof functionals, Phys. Rev. B **59**, 7413 (1999).

[43] J. Sun, A. Ruzsinszky, and J. P. Perdew, Strongly Constrained and Appropriately Normed Semilocal Density Functional, Phys. Rev. Lett. **115**, 036402 (2015).

[44] H. Rydberg, B. I. Lundqvist, D. C. Langreth, and M. Dion, Tractable nonlocal correlation density functionals for flat surfaces and slabs, Phys. Rev. B **62**, 6997 (2000).

[45] K. Berland, V. R. Cooper, K. Lee, E. Schröder, T. Thonhauser, P. Hyldgaard, and B. I. Lundqvist, van der Waals forces in density functional theory: A review of the vdW-DF method, Rep. Prog. Phys. **78**, 066501 (2015).

[46] P. Hyldgaard, Y. Jiao, and V. Shukla, Screening nature of the van der Waals density functional method: A review and analysis of the many-body physics foundation, J. Phys.: Condens. Matter **32**, 393001 (2020).

[47] H. Peng, Z.-H. Yang, J. P. Perdew, and J. Sun, Versatile van der Waals Density Functional Based on a Meta-Generalized Gradient Approximation, Phys. Rev. X **6**, 041005 (2016).

[48] E. S. Kryachko and E. V. Ludeña, Density functional theory: Foundations reviewed, Phys. Rep. **544**, 123 (2014).

[49] N. Mardirossian and M. Head-Gordon, Thirty years of density functional theory in computational chemistry: An overview and extensive assessment of 200 density functionals, Mol. Phys. **115**, 2315 (2017).

[50] G. Kresse and J. Hafner, Ab initiomolecular dynamics for liquid metals, Phys. Rev. B **47**, 558 (1993).

[51] G. Kresse and J. Hafner, Ab initiomolecular-dynamics simulation of the liquid-metal–amorphous-semiconductor transition in germanium, Phys. Rev. B **49**, 14251 (1994).

[52] G. Kresse and J. Furthmüller, Efficient iterative schemes forab initiototal-energy calculations using a plane-wave basis set, Phys. Rev. B **54**, 11169 (1996).

[53] G. Kresse and J. Furthmüller, Efficiency of ab-initio total energy calculations for metals and semiconductors using a plane-wave basis set, Comput. Mater. Sci. **6**, 15 (1996).

[54] P. E. Blöchl, Projector augmented-wave method, Phys. Rev. B **50**, 17953 (1994).

[55] G. Kresse and D. Joubert, From ultrasoft pseudopotentials to the projector augmented-wave method, Phys. Rev. B **59**, 1758 (1999).

[56] M. P. Teter, M. C. Payne, and D. C. Allan, Solution of schrödinger's equation for large systems, Phys. Rev. B **40**, 12255 (1989).

[57] A. Jain, G. Hautier, S. P. Ong, C. J. Moore, C. C. Fischer, K. A. Persson, and G. Ceder, Formation enthalpies by mixing GGA and GGA+U calculations, Phys. Rev. B **84**, 045115 (2011).

[58] A. Jain, S. P. Ong, G. Hautier, W. Chen, W. D. Richards, S. Dacek, S. Cholia, D. Gunter, D. Skinner, G. Ceder, and K. A. Persson, Commentary: The materials project: A materials genome approach to accelerating materials innovation, APL Materials **1**, 011002 (2013).

[59] J. Bandyopadhyay and K. Gupta, Low temperature lattice parameter of nickel and some nickel-cobalt alloys and grüneisen parameter of nickel, Cryogenics **17**, 345 (1977).

[60] Y. Baskin and L. Meyer, Lattice constants of graphite at low temperatures, Phys. Rev. **100**, 544 (1955).

[61] G. I. Csonka, J. P. Perdew, A. Ruzsinszky, P. H. T. Philipsen, S. Lebègue, J. Paier, O. A. Vydrov, and J. G. Ángyán, Assessing the performance of recent density functionals for bulk solids, Phys. Rev. B **79**, 155107 (2009).

[62] D. N. Batchelder and R. O. Simmons, Lattice constants and thermal expansivities of silicon and of calcium fluoride between $6°$ and $322°$K, J. Chem. Phys. **41**, 2324 (1964).

[63] M. Y. Hu, H. Sinn, A. Alatas, W. Sturhahn, E. E. Alp, H. C. Wille, Y. V. Shvyd'ko, J. P. Sutter, J. Bandaru, E. E. Haller, V. I. Ozhogin, S. Rodriguez, R. Colella, E. Kartheuser, and M. A. Villeret, Effect of isotopic composition on the lattice parameter

of germanium measured by x-ray backscattering, Phys. Rev. B **67**, 113306 (2003).

[64] M. Y. Hu, H. Sinn, A. Alatas, W. Sturhahn, E. E. Alp, H.-C. Willie, Y. V. Shvyd'ko, J. P. Sutter, J. Bandaru, E. E. Haller, V. I. Ozhogin, S. Rodriguez, R. Colella, E. Kartheuser, and M. A. Villeret, Erratum: Effect of isotopic composition on the lattice parameter of germanium measured by x-ray backscattering [Phys. Rev. B **67**, 113306 (2003)], Phys. Rev. B **69**, 079902 (2004).

[65] R. Farrow, D. Robertson, G. Williams, A. Cullis, G. Jones, I. Young, and P. Dennis, The growth of metastable, heteroepitaxial films of α-sn by metal beam epitaxy, J. Cryst. Growth **54**, 507 (1981).

[66] J. A. Rayne and B. S. Chandrasekhar, Elastic constants of β-tin from 4.2°K to 300°K, Phys. Rev. **122**, 1962 (1961).

[67] A. L. Lyubimtsev, A. I. Baranov, A. Fischer, L. Kloo, and B. A. Popovkin, The structure and bonding of Ni_3Sn, J. Alloys Compd. **340**, 167 (2002).

[68] F. Lihl and H. Kirnbauer, Untersuchung binaerer metallischer systeme mit hilfe des amalgamverfahrens. das system nickel-zinn, Monatshefte fuer Chemie **86**, 745 (1955).

[69] C. Schmetterer, H. Flandorfer, K. W. Richter, U. Saeed, M. Kauffman, P. Roussel, and H. Ipser, A new investigation of the system Ni–Sn, Intermetallics **15**, 869 (2007).

[70] P. Brand, Ueber umwandlungen in phasen vom aufgefuellten NiAs(Ni$_2$In-) strukturtyp, Z. Anorg. Allg. Chem. **353**, 270 (1967).

[71] H. Fjellvåg, A. Kjekshus, R. Stomberg, R. Zingales, I. Vikholm, F. Urso, J. Weidlein, and R. A. Zingaro, Structural properties of Co_3Sn_2, Ni_3Sn_2 and some ternary derivatives., Acta Chem. Scand. **40a**, 23 (1986).

[72] See Supplemental Material at http://link.aps.org/supplemental/10.1103/PhysRevB.105.085127 for properties of single- and multi-component systems tabulated structural and energetic properties and reduced density gradient distributions.

[73] P. Broqvist, H. Grönbeck, and I. Panas, Surface properties of alkaline earth metal oxides, Surf. Sci. **554**, 262 (2004).

[74] H. Rydberg, M. Dion, N. Jacobson, E. Schröder, P. Hyldgaard, S. I. Simak, D. C. Langreth, and B. I. Lundqvist, Van der Waals Density Functional for Layered Structures, Phys. Rev. Lett. **91**, 126402 (2003).

[75] S. Lebègue, J. Harl, T. Gould, J. G. Ángyán, G. Kresse, and J. F. Dobson, Cohesive Properties and Asymptotics of the Dispersion Interaction in Graphite by the Random Phase Approximation, Phys. Rev. Lett. **105**, 196401 (2010).

[76] K. Berland, C. A. Arter, V. R. Cooper, K. Lee, B. I. Lundqvist, E. Schröder, T. Thonhauser, and P. Hyldgaard, van der Waals density functionals built upon the electron-gas tradition: Facing the challenge of competing interactions, J. Chem. Phys. **140**, 18A539 (2014).

[77] H. W. Day, A revised diamond-graphite transition curve, Am. Mineral. **97**, 52 (2012).

[78] I. V. Popov, A. L. Görne, A. L. Tchougréeff, and R. Dronskowski, Relative stability of diamond and graphite as seen through bonds and hybridizations, Phys. Chem. Chem. Phys. **21**, 10961 (2019).

[79] F. Legrain and S. Manzhos, Understanding the difference in cohesive energies between alpha and beta tin in DFT calculations, AIP Advances **6**, 045116 (2016).

[80] J. Ihm and M. L. Cohen, Equilibrium properties and the phase transition of grey and white tin, Phys. Rev. B **23**, 1576 (1981).

[81] J. Klimeš, D. R. Bowler, and A. Michaelides, Van der Waals density functionals applied to solids, Phys. Rev. B **83**, 195131 (2011).

[82] A. Wittmann, K. O. Burger, and H. Nowotny, Mono- und disilicidsysteme der eisengruppe, Monatshefte fuer Chemie **92**, 961 (1961).

[83] M. Ellner, T. Gödecke, and K. Schubert, Zur struktur der mischung nickel-germanium, J. Less-Common Met. **24**, 23 (1971).

[84] T. Y. Velikanova, A. A. Bondar, and A. V. Grytsiv, The chromium-nickel-carbon (Cr-Ni-C) phase diagram, JPE **20**, 125 (1999).

[85] M. Singleton and P. Nash, The C-Ni (carbon-nickel) system, Bull. Alloy Phase Diagrams **10**, 121 (1989).